

Article

{CeO₂/Bi₂Mo_{1-x}Ru_xO₆} and {Au/Bi₂Mo_{1-x}Ru_xO₆} Catalysts for Low-Temperature CO Oxidation

Edson Edain González ¹, Ricardo Rangel ^{1,*}, Javier Lara ¹, Pascual Bartolo-Pérez ²,
Juan José Alvarado-Gil ², Donald Homero Galván ³ and Rafael García ⁴

- ¹ División de Estudios de Posgrado de la Facultad de Ingeniería Química, Universidad Michoacana de San Nicolás de Hidalgo, Gral. Francisco J. Múgica S/N, Ciudad Universitaria. Z. C. 58030 Morelia, Michoacán, Mexico; eega_ibq@hotmail.com (E.E.G.); jlara_romero@hotmail.com (J.L.)
- ² Departamento de Física Aplicada, CINVESTAV, Unidad Mérida, Antigua Carretera a Progreso Km. 6, Cordemex. Z. C. 97310 Mérida, Yucatán, Mexico; pascual@cinvestav.mx (P.B.-P.); jjag09g@gmail.com (J.J.A.-G.)
- ³ Centro de Nanociencias y Nanotecnología, Universidad Nacional Autónoma de México, Z. C. 22800 Ensenada, B.C., Mexico; donald@cryn.unam.mx
- ⁴ Departamento de Investigación en Física, Universidad de Sonora, 83000 Hermosillo, Sonora, Mexico; rafael.gutierrez@unison.mx
- * Correspondence: rrangel@umich.mx; Tel.: +52-443-327-3584

Received: 8 October 2019; Accepted: 6 November 2019; Published: 12 November 2019



Abstract: Nowadays, one of the most important challenges that humanity faces is to find alternative ways of reducing pollutant emissions. CeO₂/Bi₂Mo_{1-x}Ru_xO₆ and Au/Bi₂Mo_{1-x}Ru_xO₆ catalysts were prepared to efficiently transform carbon monoxide (CO) to carbon dioxide (CO₂) at low temperatures. The systems were prepared in a two-step process. First, Bi₂Mo_{1-x}Ru_xO₆ supports were synthesized through the hydrothermal procedure under microwave heating. Then, CeO₂ was deposited on Bi₂Mo_{1-x}Ru_xO₆ using the wet impregnation method, while the incipient impregnation method was selected to deposit gold nanoparticles. The CeO₂/Bi₂Mo_{1-x}Ru_xO₆ and Au/Bi₂Mo_{1-x}Ru_xO₆ catalysts were characterized using SEM microscopy and XRD. Furthermore, energy-dispersive X-ray spectroscopy (EDS), X-ray photoelectron spectroscopy (XPS), and Raman spectroscopy were used. Tests were carried out for the supported catalysts in CO oxidation, and high conversion values, nearing 100%, was observed in a temperature range of 100 to 250 °C. The results showed that the best system was the Au/Bi₂Mo_{0.95}Ru_{0.05}O₆ catalyst, with CO oxidation starting at 50 °C and reaching 100% conversion at 186 °C.

Keywords: CO oxidation; CeO₂; Au; Bi₂Mo_{1-x}Ru_xO₆; nanostructured catalysts

1. Introduction

The drastic growth in atmospheric pollution is the product of industrial development as well as the increasing use of automobiles for transportation, which in turn maintains a growing demand for fossil fuels. It is an important and still pending task to decrease the atmospheric pollutants coming from these processes, including CO_x, SO_x, and NO_x, which significantly contribute to the phenomena of acid rain, global warming, and destruction of the ozone layer [1]. Carbon monoxide (CO) is considered highly poisonous, and it causes severe health issues and irreversible environmental damage [2]. In this context, the development of materials with high activity for removing CO becomes necessary. Traditional supported noble metal catalysts are examples of materials with excellent catalytic properties to promote CO oxidation at low temperatures [3,4].

Bi₂MoO₆ is recognized as a good catalyst, and it is useful in selective oxidation processes [5]. The most common methods to synthesize it include coprecipitation [6,7], followed by calcination

processes or through solid-state reactions [8] at temperatures above 1000 °C. Alternatively, Bi_2MoO_6 can also be obtained by sol-gel synthesis [9] or spray-drying methods [10]. The catalytic properties of bismuth molybdate are well known. For instance, in propane transformation reactions, it is considered an essential component [6,11], even though some of its phases are not active, as has been reported by Ueda et al. [12]. Schuh et al. [13] investigated the selectivity of several bismuth molybdates in propylene oxidation reaction using $\alpha\text{-Bi}_2\text{Mo}_3\text{O}_{12}$, $\beta\text{-Bi}_2\text{Mo}_2\text{O}_9$, and $\gamma\text{-Bi}_2\text{MoO}_6$ phases. When testing the $\gamma\text{-Bi}_2\text{MoO}_6$ catalyst containing an excess of stoichiometric bismuth/molybdenum in a 3:1 ratio, the authors obtained results for propylene conversion of up to 7.3%. However, the selectivity toward acrolein formation was very low, and mainly CO_x was formed. Compounds with a Bi/Mo ratio of 3:1 was found to produce a $\alpha\text{-Bi}_2\text{Mo}_3\text{O}_{12}$ compound exhibiting acrolein selectivity in the range of 36%–56%, providing a 60%–63% propylene conversion. Brazdil et al. [14] reported on the synthesis of bismuth–cerium molybdate compounds with a $\text{Bi}_x\text{Ce}_{2-x}\text{Mo}_3\text{O}_{12}$ formulation. They studied the selectivity as a function of cerium content, to prove its effectiveness in reactions for catalytic propylene ammoxidation. Their results allowed them to establish active sites as a function of the bismuth content for propylene ammoxidation. Other investigations have been conducted using $\text{Bi}_2\text{Mo}_x\text{W}_{1-x}\text{O}_6$ supported on $\text{Al}_2\text{O}_3\text{-SiO}_2$, which were tested in carbon monoxide oxidation reaction to evaluate its activation temperature. The compounds were found to activate at 200 °C, reaching 100% conversion at about 350 °C [15]. Furthermore, there have been investigations based on the dehydrogenation of organic compounds using catalysts composed of mixed oxides containing molybdenum, bismuth, and vanadium. The studies examined their catalytic activity and determined how the bismuth–molybdate structure is modified when it is doped with a metal. In a temperature-programmed reoxidation experiment, they established that catalysts containing vanadium exhibited enhanced oxygen mobility in comparison to Bi_2MoO_6 , showing an important 1-butene to 1,3-butadiene catalytic conversion (72%) in oxidative dehydrogenation reactions [16,17].

Ruthenium is not a widely used metal in oxidation reactions due to its low melting point as RuO_2 . However, its high reactivity toward carbon monoxide oxidation has become a point of interest in the field of catalysis. In this regard, studies have been conducted on ruthenium in relation to their particle size, which ranges from 2 to 6 nm, using polyvinylpyrrolidone (PVP) as the size-regulating agent. The results showed that, as Ru nanoparticles became smaller, they began to be more active and efficient in CO to CO_2 conversion [18]. Another reaction in which ruthenium is used as a catalyst is in the heterogeneous oxidation of alcohols. To induce these reactions, ruthenium is obtained by coprecipitation processes and deposited on Al_2O_3 metal supports being activated in an oxygen-rich atmosphere [19]. Ruthenium nanoparticles deposited on cerium oxide has also been reported, with the studies concluding that a relatively large CeO_2 surface area favors ruthenium particle dispersion, increasing its catalytic activity in CO oxidation reaction [19,20]. Unfortunately, RuO_2 is not stable unless it is stabilized by the addition of some external element, which makes its use technically complicated. The key to the widespread use of RuO_2 is therefore to find a way to achieve such stabilization.

In the last few decades, researchers have studied the catalytic properties of supported gold catalysts for CO oxidation. Au nanoparticles have been successfully tested in carbon monoxide oxidation reactions at low temperatures [21]. One of the first investigations carried out on the synthesis of gold nanoparticles was performed by Haruta [22], who reported the production of synthesized particles smaller than 10 nm and deposited on oxide supports for its use in hydrogen and carbon monoxide oxidation reactions. Other investigations examined the use of gold nanoparticles deposited on ceria nanotubes and obtained good results in catalytic oxidation reactions [23]. Such materials perform an important role in catalyzing different reactions at low temperatures. This feature is attributed to the presence of low-coordinate gold atoms on the surface of CeO_2 nanoparticles [24]. CeO_2 powder has been listed as one of the best supporting materials for catalysis when it is associated with gold nanoparticles as an active phase due to its relevant storage and oxygen-releasing capability [25]. An important feature attributed to CeO_2 compounds, is the formation of vacancies within the crystalline structure, when doping is carried out because these could modify the entropy and increase its thermodynamic

stability. These features are relevant as they determine the speed at which ions can move through their surface [26], providing bandgap narrowing, which in turn promotes the transference of electrons from the valence to the conduction band [21,25,27,28]. The oxidative capability of cerium oxide has been widely demonstrated through several studies on CO oxidation reactions, used either as an active phase [5] or as a support in noble metal catalysts [25]. Furthermore, specific studies on nanostructured CeO₂ powders in the form of rods exposing predominantly (111) surfaces and cubes exposing (100) surfaces have been reported. In those studies have been reported that Pd deposited on the (111) plane of ceria rods, exhibited CO conversion at room temperature, while Pd on (100) ceria cubes showed similar CO conversion values at 60 °C. The differences found in CO conversion can be attributed to Pd redispersion, which is more pronounced in oxidative conditions for Pd/CeO₂ rods [29].

The results already discussed related to CeO₂, RuO₂, Au nanoparticles, and Bi₂MoO₆ used as catalysts in CO oxidation reaction, supports the hypothesis that different prepared materials including oxides as CeO₂/Bi₂Mo_{1-x}Ru_xO₆ (OCMBR) and Au/Bi₂Mo_{1-x}Ru_xO₆ (AuMBR), could oxidize efficiently CO to CO₂. It is also important to elucidate the synergistic relationship between the active phases and the mixed oxide support to promote CO to CO₂ conversion at low temperatures.

2. Results

2.1. Scanning Electron Microscopy (SEM)

The morphology of the MBR supports and OCMBR and AuMBR catalysts are shown in Figure 1a,b and Figure 1c–f, respectively. In Figure 1a,b, granular and small rounded structures can be observed. The 500 nm particles had a similar shape but different distributions. In the case of Bi₂Mo_{0.95}Ru_{0.05}O₆ (MBR1), there was formation of agglomerations, while the particles were smaller in Bi₂Mo_{0.97}Ru_{0.03}O₆ (MBR2). Figure 1c–f shows OCMBR and AuMBR catalysts consisting of rounded particles (< 70 nm) obtained as a result of using the PVP surfactant agent. In this case, the particles had an average size of approximately 100 nm.

Table 1 shows the chemical composition of the catalysts (Ce, Au, Bi, Mo, O, Ru). The chemical content was determined by energy-dispersive X-ray spectroscopy (EDS). The atomic concentration of the species corresponding to bismuth molybdate remained constant, with a high concentration of oxygen. It is important to mention that the quantification performed for Au and Ce showed values close to 1.5 atomic percent (at %) which is lower than the expected 2 (at %) content. This could be attributed to some loss during the deposition or washing processes. In the case of cerium, the values exceeded only 3 at %.

Table 1. Elemental chemical analysis (atomic percent) obtained by energy-dispersive X-ray spectroscopy (EDS) using an EDAX detector.

Sample	Chemical Composition (Atomic Percent)					
	Bi	Mo	Ru	O	Ce	Au
MBR1	22.05	13.62	1.56	64.34	-	-
MBR2	29.81	12.56	1.49	57.63	-	-
OCMBR1	16.1	13.65	2.12	64.67	3.46	-
OCMBR2	16.72	13.47	1.89	64.95	3.21	-
AuMBR1	16.04	19.34	1.69	61.73	-	1.2
AuMBR2	14.49	22.29	1.35	60.54	-	1.33

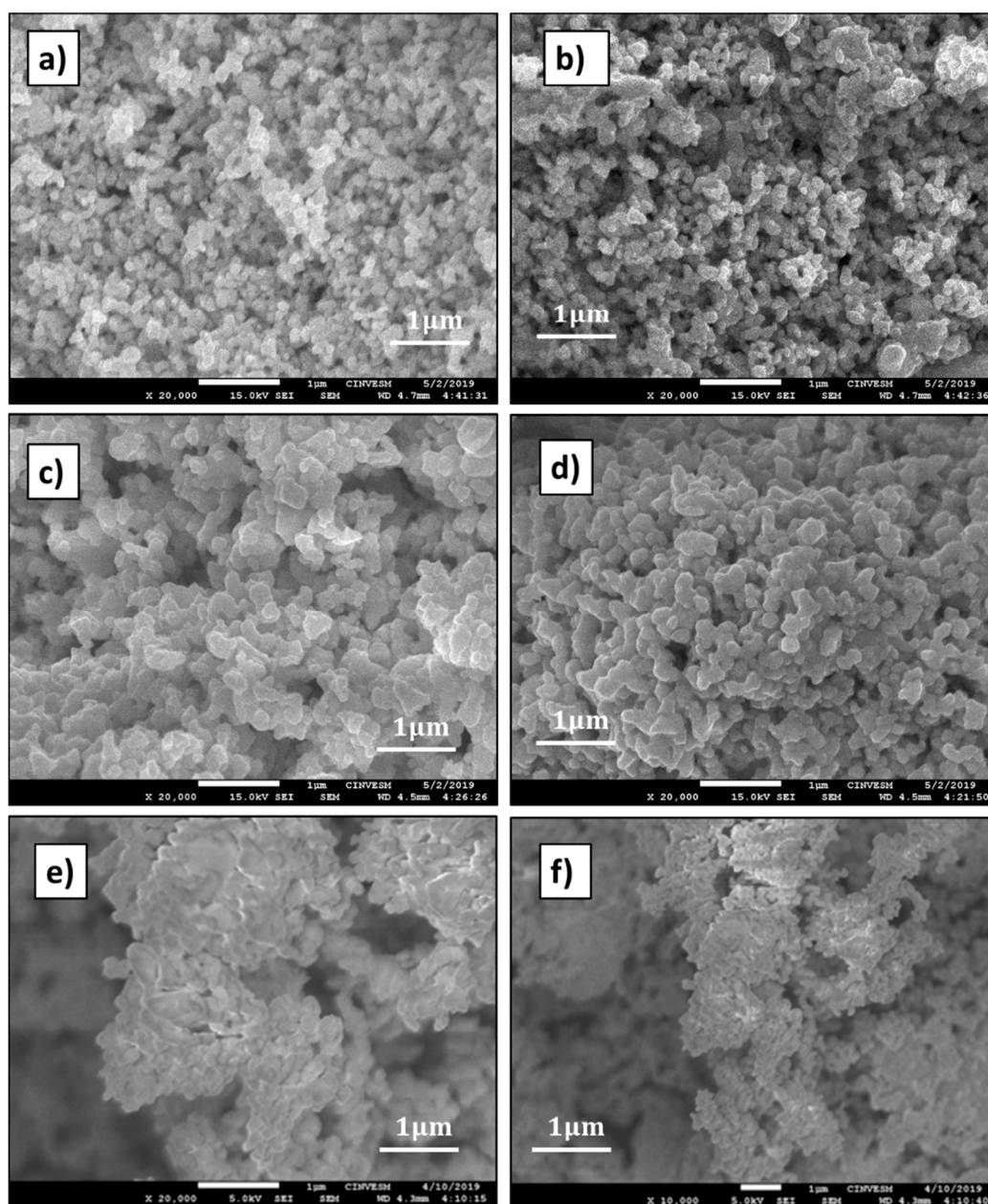


Figure 1. Scanning electron microscopy (SEM) images of (a) $\text{Bi}_2\text{Mo}_{0.95}\text{Ru}_{0.05}\text{O}_6$ (MBR1); (b) $\text{Bi}_2\text{Mo}_{0.97}\text{Ru}_{0.03}\text{O}_6$ (MBR2); (c) $\text{CeO}_2/\text{Bi}_2\text{Mo}_{0.95}\text{Ru}_{0.05}\text{O}_6$ (OCMBR1); (d) $\text{CeO}_2/\text{Bi}_2\text{Mo}_{0.97}\text{Ru}_{0.03}\text{O}_6$ (OCMBR2), (e) $\text{Au}/\text{Bi}_2\text{Mo}_{0.95}\text{Ru}_{0.05}\text{O}_6$ (AuMBR1), and (f) $\text{Au}/\text{Bi}_2\text{Mo}_{0.97}\text{Ru}_{0.03}\text{O}_6$ (AuMBR2) compounds under a magnification of 20,000X.

2.2. X-Ray Diffraction (XRD)

X-ray diffraction patterns of the synthesized compounds, including the doped ruthenium catalytic support and the catalysts after impregnation, are shown in Figure 2. The signal corresponding to the 2θ angle of 28.34° can be attributed to the (131) plane characteristic of the Bi_2MoO_6 gamma phase, which has an orthorhombic-like structure. Two other signals located at 32.51° (200) and 47.10° (260) were also found (Figure 2f).

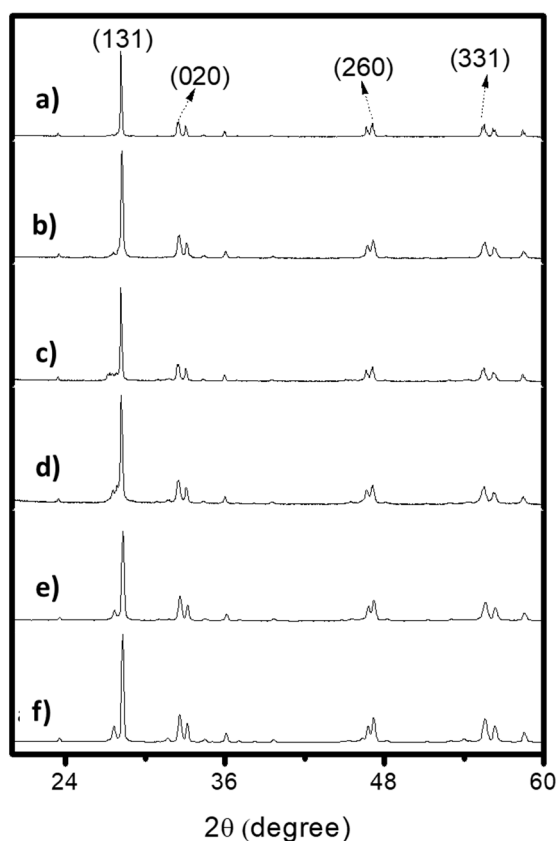


Figure 2. X-ray diffraction patterns of (a) AuMBR1; (b) AuMBR2; (c) OCMBR2; (d) OCMBR1; (e) MBR2; and (f) MBR1 synthesized catalysts. Cu K α radiation operating with a step size of 0.02°/min from 10° to 90°.

The synthesis allowed correct ruthenium incorporation into the catalytic support structure [30]. This was verified through the signal displacement of the (131) plane toward greater angles (Figure 2a,b).

Regarding the OCMBR compounds, their X-ray diffraction pattern showed a signal located at 28.4° (2 θ), as shown in Figure 2c,d. The signal can be attributed to the CeO₂ (111) plane, in agreement with results previously reported by other authors [31]. For the Au/Bi₂Mo_{0.95}Ru_{0.05}O₆ (AuMBR1) catalyst, characteristic peaks of the gamma phase of bismuth molybdate (γ -Bi₂MoO₆) were found. Their main characteristic peak located at 28.3° (Figure 2e) can be attributed to the (131) crystalline plane, on which it obtained a crystal size of 37.9 and 37 nm for MBR1 and MBR2, respectively. These values can be obtained through the Scherrer equation:

$$D = \frac{K\lambda}{W \cos \theta} \quad (1)$$

where K is a constant that depends on particle morphology (usually $K = 1$ for cubic or nearly cubic systems), λ is the Cu K α radiation (nm), W is the full width at half maximum (rad), and θ is the diffraction angle (deg).

2.3. X-Ray Photoelectron Spectroscopy (XPS)

The XPS technique was used to detect the presence of different chemical species involved in our catalysts. The binding energy (BE) analysis for the chemical species of the support revealed signals at 530.57, 527.4, and 529.9 eV for oxygen (O1s). The peaks for Mo3d and Bi4f were also detected. The signals for Mo⁺⁶ were obtained at 235.66 and 232.63 eV [32]. In addition, the signals for Bi⁺³ were observed at 164.63 and 159.37 eV (Figure 3) [30,33]. An XPS signal, located at 280 eV, was found corresponding to Ru3d_{5/2}. This is often confused with carbon signal, but a high-resolution analysis

performed for this compound confirmed its presence (Figure 4). This BE signal matched Ru^{+4} [34] and was detected at 280.6 and 280.3 eV. These signals can be attributed to the presence of Ru–O bonds within the $\text{Bi}_2\text{Mo}_{1-x}\text{Ru}_x\text{O}_6$ structure. This outcome agrees with the results discussed in the XRD section, where the ruthenium oxide phase was not found, similar to previous findings [35].

Figure 5 shows the XPS analysis for $\text{CeO}_2/\text{Bi}_2\text{Mo}_{0.95}\text{Ru}_{0.05}\text{O}_6$ (OCMBR1) and $\text{CeO}_2/\text{Bi}_2\text{Mo}_{0.97}\text{Ru}_{0.03}\text{O}_6$ (OCMBR2) supported catalysts. In addition to Bi, Ru, and O, the representative signal of cerium (Ce3d) with a BE of 886.08 eV, corresponding to the Ce–O interaction in CeO_2 , was established [36–38].

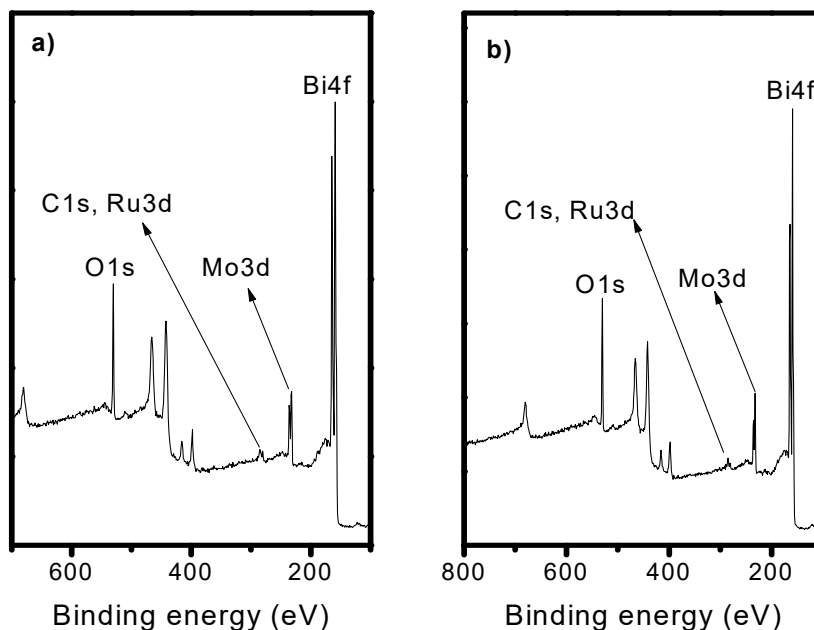


Figure 3. General X-ray photoelectron spectroscopy (XPS) scan of (a) MBR1 and (b) MBR2 support catalysts.

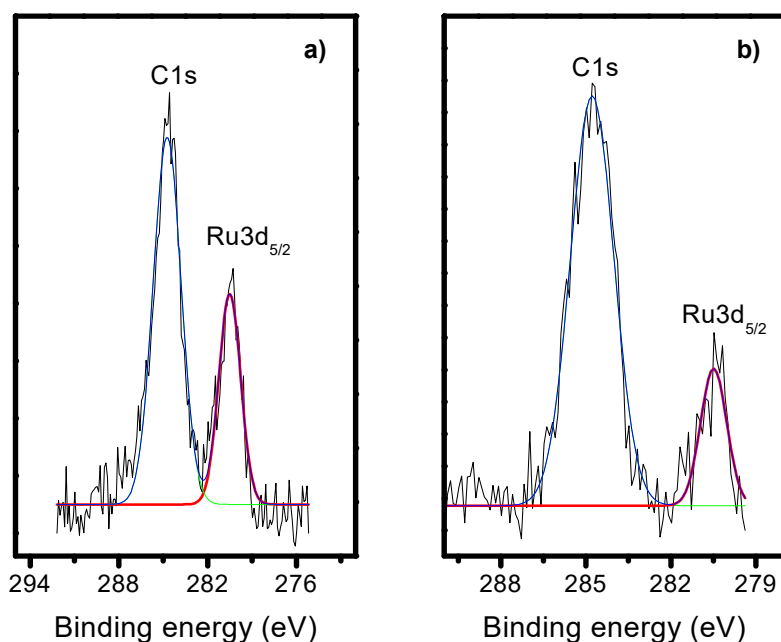


Figure 4. High-resolution XPS analysis for Ru3d of (a) MBR1 and (b) MBR2 supports.

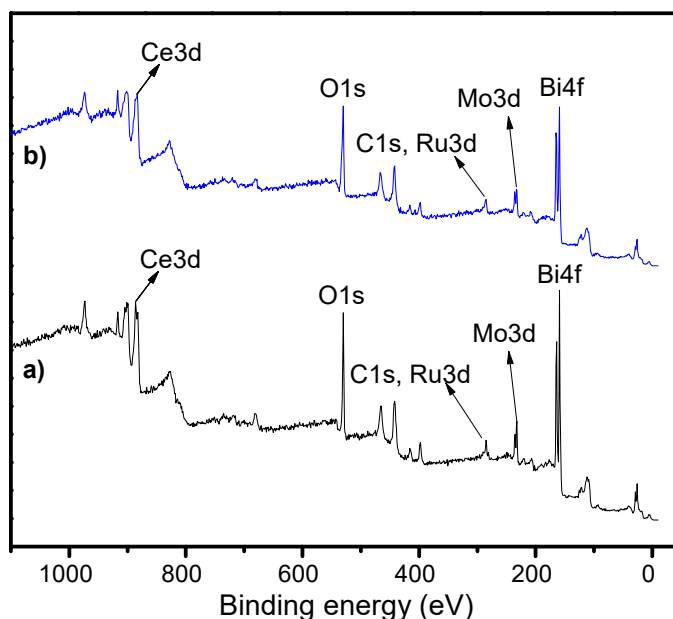


Figure 5. General XPS scans of (a) OCMBR1 and (b) OCMBR2 catalysts.

Figure 6 shows the XPS scans of AuMBR catalysts, where Bi, Ru, O, and Au signals were detected. The oxidation state for every element present was matched according to established standards. In addition, a high-resolution energy spectrum for gold was performed to obtain signals for the different oxidation states present. The results showed the presence of gold as Au^{+3} and Au^0 . The corresponding XPS curves of Au spectra of the Au/MBR catalysts are shown in Figure 7a–d. The characteristic signals for Au^0 and Au^{+3} were found at the BE of 84 and 87.43 eV values, respectively, which were assigned to Au $4f_{7/2}$ and Au $4f_{5/2}$ signals. The $4f_{7/2}$ signal revealed that the Au was in a metallic valence, while the $4f_{5/2}$ signal was attributed to its ionic state [39,40]. The results of the deconvolution procedure to establish the amount of Au^{+3} and Au^0 are summarized in Table 2.

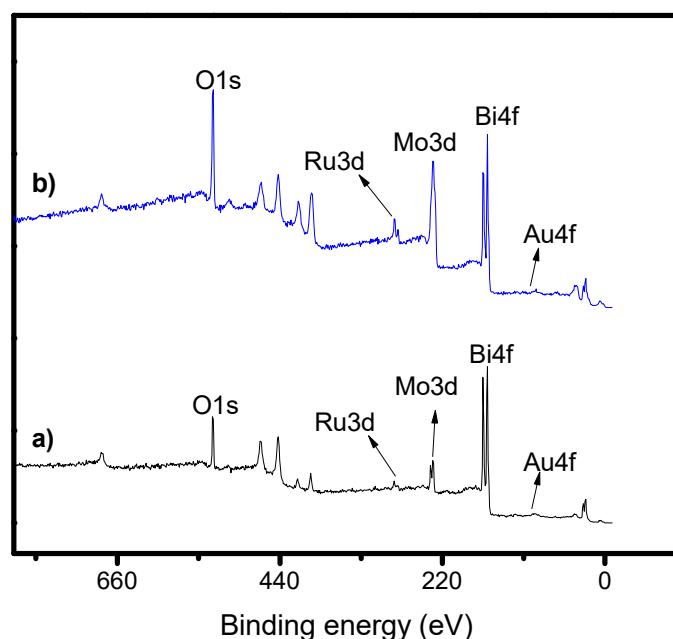


Figure 6. General XPS scans of (a) AuMBR1 and (b) AuMBR2 catalysts.

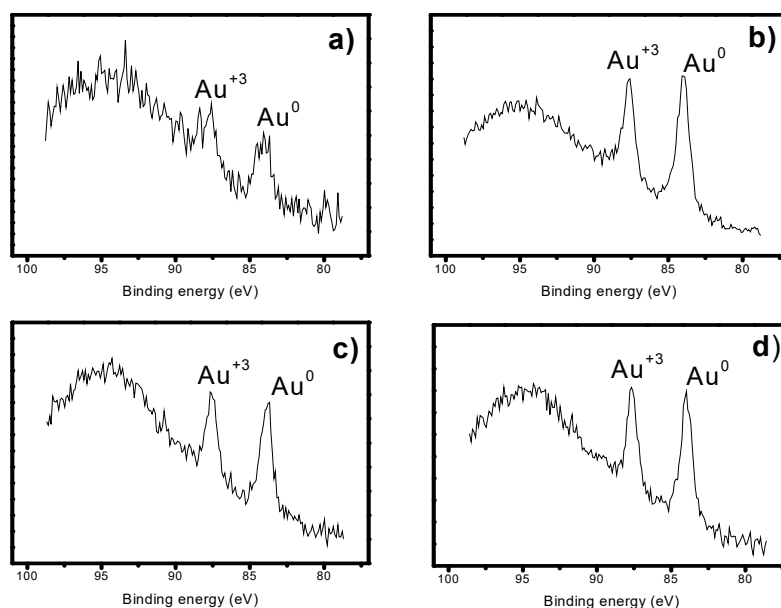


Figure 7. High-resolution XPS analysis of Au4f of (a) AuMBR1; (b) AuMBR1_R; (c) AuMBR2; and (d) AuMBR2_R (R: reduced).

Table 2. Quantification of chemical gold species before and after reduction with H₂.

Catalysts		Au Species (%)	
		Au ⁺³	Au ⁰
AuMBR1	Before reduction	61.34	38.66
	After reduction	39.24	60.76
AuMBR2	Before reduction	45.03	54.97
	After reduction	38.56	61.44

To increase the presence of Au⁰ in both AuMBR1 and Au/Bi₂Mo_{0.97}Ru_{0.03}O₆ (AuMBR2) catalysts, they were subjected to a reduction process using H₂ at 500 °C for 4 h. The results for Au⁺³ and Au⁰ are shown in Table 2 and also in Figure 7b,d [41–43].

After reducing each AuMBR catalyst with H₂, the atomic quantification of each species was performed, as shown in Figure 7. Table 2 gives the results of Au⁰ content before and after carrying out the reduction process. It can be observed that, for the AuMBR1 catalyst, the Au⁺³ percentage was higher than that of Au⁰ before reduction. Once the reduction process was carried out, the Au⁰/Au⁺³ ratio increased, thus obtaining a higher amount of Au⁰. The corresponding analyses for the reduced samples—AuMBR1_R and AuMBR2_R—are shown in Figure 7b,d. As can be seen, the Au⁰ content increased by about 30 %. The oxidative capacity of the catalysts was studied before and after the reduction procedure, and their corresponding values will be discussed later.

2.4. Raman Spectroscopy

Figure 8 shows the spectrum obtained for MBR supports, with their vibrational characteristic mode values located at 68.16, 131.86, 788.78, and 880.8 cm⁻¹. Similar results have been reported by other authors, establishing that very strong vibrational modes are observed for Bi₂MoO₆ at 808 cm⁻¹ as well as two minor peaks at 852 and 722 cm⁻¹, corresponding to Mo–O stretches of the distorted MoO₆ octahedra [44]. Additionally, two signals found at 356 and 283 cm⁻¹, which can be ascribed to the Bi–O–Mo or Bi–O vibrational modes [34,35,45,46], were shown in the Raman spectra when a β-Bi₂MoO₆ phase was detected. The Ru characteristic band with Ru–O vibrational modes can be found at 310 cm⁻¹ [36,41]. As can be seen from Figure 8, the ruthenium content promoted the shifting from 299.73 to 301.72 cm⁻¹.

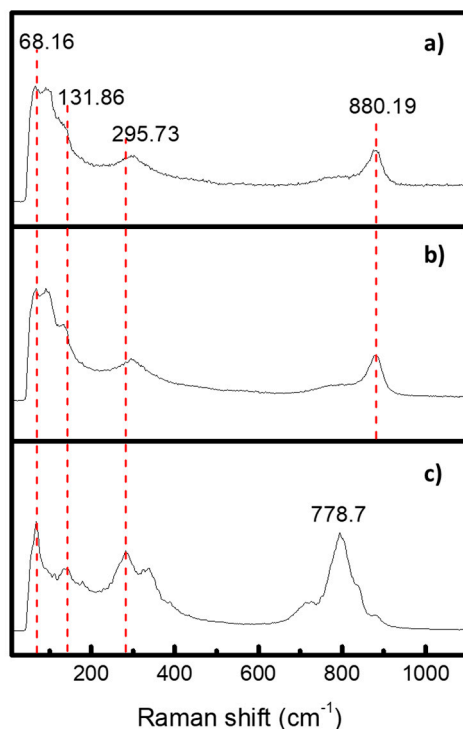


Figure 8. Raman spectra of (a) MBR2; (b) MBR1; and (c) Bi_2MoO_6 compounds.

2.5. Catalytic Activity Tests

In this section, the results obtained for tests carried out on the capacity of the developed compounds for carbon monoxide oxidation as a function of temperature are presented. MBR1 and MBR2 supports showed an improvement in comparison to pristine Bi_2MoO_6 (MB), as previously reported [5]. MB showed its activation at 220 °C, reaching 98% CO oxidation at 380 °C. The MB support never reached 100% conversion, as can be seen in Figure 9, which means that the support decreases its oxidative capacity at a temperature above 300 °C. In comparison, MBR1 and MBR2 compounds started their activation under 150 °C and reached 98% CO oxidation at 220 °C, demonstrating an improvement due to ruthenium inclusion. The difference in conversion capacity between MB and MBR catalysts can be attributed to the atomic content of ruthenium in the MBR supports, in accordance with previously reported results [42].

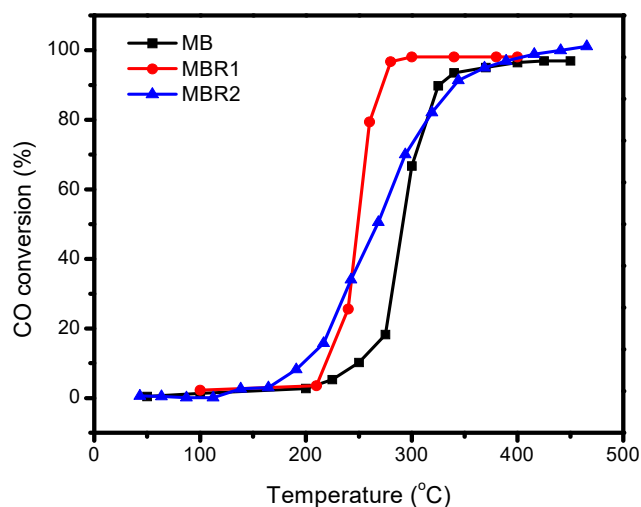


Figure 9. Comparative graph of CO conversion percentage for MB, MBR1, and MBR2 catalysts.

Figure 10 shows the CO conversion behavior of AuMBR and OCMBR catalysts. The OCMBR1 catalyst was activated at 150 °C, reaching 100% conversion at 250 °C, while the OCMBR2 catalyst was activated at 175 °C and reached 100% CO conversion at 275 °C. The OCMBR catalysts were found to be more efficient in CO conversion than MBR catalytic supports, being activated at 95 °C and reaching 100% CO conversion at 280 °C. This is related to the oxidative capacity of ceria, which works synergistically with the $\text{Bi}_2\text{Mo}_{1-x}\text{Ru}_x\text{O}_6$ compound [47]. Venkataswamy et al. [48] performed work on Mn–ceria-doped solid solutions used as catalysts in CO oxidation reactions at low temperatures. They observed that Mn–ceria catalysts were activated at 50 °C, reaching 100% conversion at a temperature higher than 320 °C. It is necessary to highlight that OCMBR catalysts, in spite of being a highly active compound in CO oxidation [21,49], were not the ones with the best results, as shown in the conversion graph.

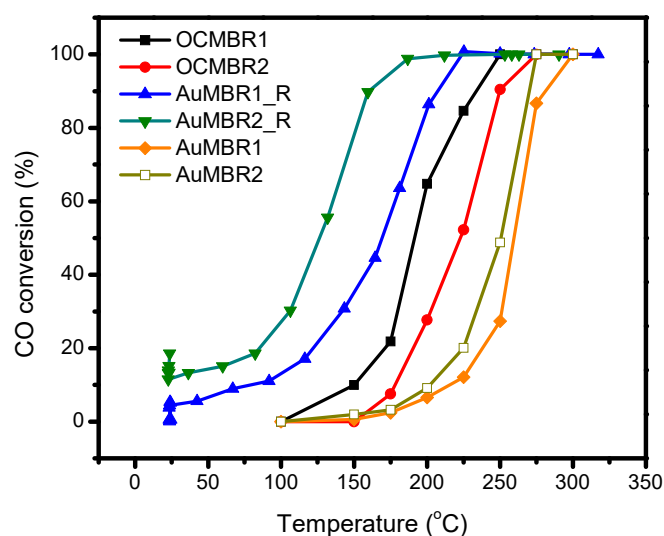


Figure 10. Comparative graph of CO conversion for OCMBR1, OCMBR2, AuMBR1_R, AuMBR2_R, AuMBR1, and AuMBR2 catalysts. (R: reduced).

As described in the section on XPS analysis, AuMBR catalysts showed a higher concentration of Au^{+3} in comparison to Au^0 . Based on the analysis, it can be inferred that the catalysts underwent a reduction with hydrogen to increase the Au^0 concentration (see Table 2). The reduced catalysts were labeled as AuMBR_R. Figure 10 shows the results of CO conversion for the nonreduced catalysts and the reduced ones. It can be observed that the AuMBR1 and AuMBR2 catalysts were activated at 150 °C, reaching 100% conversion at 275 °C and 300 °C, respectively. In the case of the reduced catalysts—AuMBR1_R and AuMBR2_R—they were activated at 23 °C. The AuMBR1_R catalyst reached 100% CO conversion at 186 °C, while the AuMBR2_R catalyst reached it at 225 °C. There was substantial change in terms of oxidative capacity of the gold supported catalysts when they underwent a reduction process. This means that a higher $\text{Au}^0/\text{Au}^{+1}$ ratio, obtained through the reduction process, improves CO oxidation [18,21,50].

3. Discussion

Several studies have been carried out to understand how CO molecules interact with Au particles supported on ZnO [51]. According to the obtained results, the oxidation process starts with a process of CO adsorption taking place in CO/Au/ZnO complexes in specific sites formed by Au clusters following the Mars–van Krevelen (MvK) kinetic model [52]. AuMBR catalysts work similarly, carrying out the CO oxidation process through a MvK kinetic model in synergy with the oxidative capability of the MBR ($\text{Bi}_2\text{Mo}_{1-x}\text{Ru}_x\text{O}_6$) support, which enhances the transport efficiency of electrons toward the surface, thereby improving the oxidative activity of Au particles. The formation of the complex CO/Au/ $\text{Bi}_2\text{Mo}_{1-x}\text{Ru}_x\text{O}_6$ is believed to happen in the same order as the MvK mechanism.

Regarding the OCMBR catalysts, the reaction mechanism follows a consecutive series of elementary steps that include a constant change in the cerium valence ($\text{Ce}^{+3} \leftrightarrow \text{Ce}^{+4}$) due to changes in oxygen concentration occurring within the OCMBR structure. In CO oxidation reactions, the oxygen storage capability of CeO_2 catalysts has been demonstrated. Oxygen located at the catalyst surface oxidize the CO molecules, while the introduced bimolecular oxygen decomposes according to the Langmuir-Hinshelwood mechanism to fill the vacancies created by the CO oxidation reaction [53].

Investigations with Au nanoparticles have reported obtaining compounds capable of being activated at 0 °C. However, they do not reach a high conversion rate until temperatures above 300 °C [17,43,54]. In the case of compounds in which Au acts as active phase (Au/TiO_2 , Au/NiO , $\text{Au}/\alpha\text{-Fe}_2\text{O}_3$), catalysts show a disadvantage because the formation of water vapor at high temperatures increases to the point of reducing the oxidative activity of the Au nanoparticles, as shown by other similar reports [21,23,38,41]. An important challenge in the present research was to ensure that most of the dispersed gold particles on the $\text{Bi}_2\text{Mo}_{1-x}\text{Ru}_x\text{O}_6$ surface supports could be found in the metallic oxidation state (Au^0) to further increase its oxidative behavior. Our XPS analysis demonstrated that gold was found in Au^{+1} and Au^0 oxidation states, with Au^0 more predominant, providing our catalysts an outstanding oxidative capacity. This was demonstrated in the catalytic activity tests, where AuMBR1 reached 100% CO oxidation at 150 °C. Furthermore, in our studies, metallic particles smaller than 10 nm in size were obtained, which is a determining feature to achieve the CO oxidation reaction, as previously discussed by Zhang et al. [55] and Kimling et al. [56]. The results here discussed are encouraging for continued work on the optimization of our systems.

4. Materials and Methods

4.1. Catalysts Preparation

MBR1 and MBR2 solid solutions were prepared starting with aqueous solutions of $(\text{NH}_4)_6\text{Mo}_7\text{O}_{24}$ (97%, Alyt), $\text{Bi}(\text{NO}_3)_3$ (99.99%, Alfa Aesar), and $\text{Ru}_3(\text{CO})_{12}$ (99%, Alfa Aesar), which were mixed in a stoichiometric ratio. PVP was also added into the mixture as a capping agent to control particle size. The mixture was stirred for about two hours at 30 °C. Then, the solid solution was formed using hydrothermal treatment assisted by microwave heating at 150 °C for 1 h. The resulting powder was washed with 5 mL of isopropanol, dried at 120 °C for 24 h, and then heated at 500 °C for 3 h. The supported systems—AuMBR1 and AuMBR2—were obtained using HAuCl_4 solution 0.0016 M as a gold precursor and urea 0.42 M, through the deposit–precipitation (DP) urea method [57]. The Au/catalyst ratio was calculated as 1% (w/w).

Regarding OCMBR1 and OCMBR2 catalysts, they were prepared via wet impregnation using a 0.23 M $\text{Ce}(\text{NO}_3)_3$ solution. The stoichiometric ratio of the active phase to the support was nearly 4% (w/w).

After performing the impregnation procedure, all of the catalysts were dried at 120 °C for 12 h and calcined at 550 °C for 3 h. Before the catalytic tests, AuMBR1 and AuMBR2 catalysts were reduced at 400 °C for 4 h in a $30 \text{ cm}^3 \text{ min}^{-1}$ hydrogen flow.

4.2. Characterization

SEM images were obtained using a JEOL JSM 5300 scanning electron microscope Noran Instruments (Japan), coupled with an energy-dispersive analyzer (EDAX) also provided by Noran Instruments (Japan) operating at 20 kV and 1×10^{-6} Torr. X-ray diffraction analyses were obtained in a Philips X'Pert analytical diffractometer (England) using $\text{Cu K}\alpha$ radiation under conditions of 40 kV voltage and 30 mA current. Before the analysis, the catalysts were ground in an agate mortar and passed through a 100-mesh sieve (Tyler series). The XPS technique allowed the oxidation states to be determined, in which the main elements were found using a Thermo Scientific equipment with an X-ray source provided with an $\text{Al-K}\alpha$ monochromator (MA, USA). The analysis area was $400 \mu\text{m}^2$. Before starting the analysis, the surface was eroded with low-energy Ar ions for 15 s to eliminate possible surface

impurities. Raman spectroscopy analyses were performed on a Witec Alpha 300 device (Germany) using a laser as the illumination source (633 nm) provided with a charge-coupled device (CCD) detector for the measurement of scattered Raman emission.

4.3. Catalytic Assessment

The CO oxidation reaction was carried out in a packed microflow quartz reactor, 8 mm diameter, under atmospheric pressure in a range of 20–350 °C. The CO to O₂ ratio was adjusted to CO/O₂ = 1 with a rate of 60 mL/min (2% CO, 2% O₂, 96% Ar). The catalyst weight was 100 mg. Before the tests, catalysts were pretreated (activated) at 300 °C with a mixture of H₂/N₂ gases in a 2%/90% v/v ratio, for 1 h. The reaction products were analyzed using thermal conductivity gas chromatography provided with a carboxen-1000 column (1/8 inch diameter and 4 m long) using a thermal conductivity detector (TCD) to determine the reaction products, as described in Figure 11.

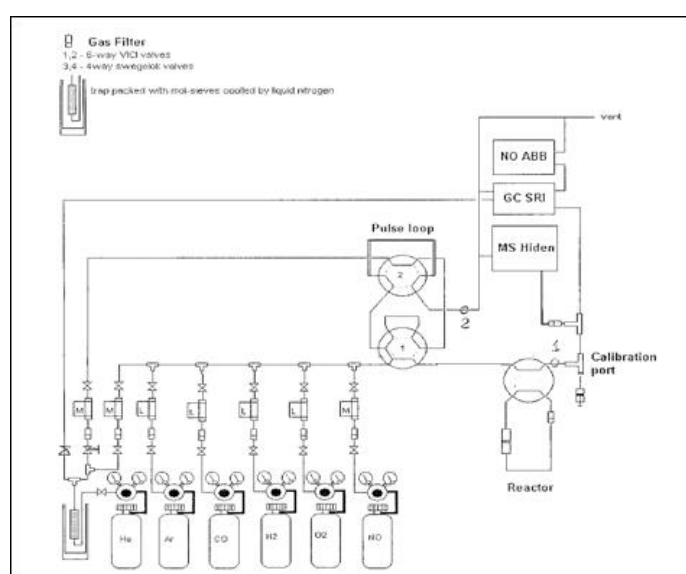


Figure 11. Schematic flow diagram of the reaction system.

5. Conclusions

In the present study, the oxidative capability of CeO₂/Bi₂Mo_{1-x}Ru_xO₆ and Au/Bi₂Mo_{1-x}Ru_xO₆ catalysts were demonstrated. It was found that the ruthenium inclusion as Bi₂Mo_{1-x}Ru_xO₆ improved the oxidative behavior compared to Bi₂MoO₆. The Bi₂Mo_{1-x}Ru_xO₆ compound achieved 100% CO conversion at 260 °C, which can be considered an improvement compared to the Bi₂MoO₆ compound, which achieved 95% CO conversion at 375 °C. Regarding the supported catalysts, a synergistic effect was observed between the active phase and the catalytic support. The CeO₂/Bi₂Mo_{1-x}Ru_xO₆ system showed an improvement, with OCMBR1 starting CO conversion at a temperature of 120 °C and reaching 100% conversion to CO₂ at 225 °C. With the Au/Bi₂Mo_{1-x}Ru_xO₆ catalytic systems, it started oxidizing CO at a temperature as low as 23 °C, reaching 100% CO conversion at a temperature of 180 °C. The Au/Bi₂Mo_{0.97}Ru_{0.03}O₆ compound was found to be the best catalyst to oxidize CO at low temperatures. Further optimization studies are needed regarding the stability and oxidative capability of Au and CeO₂ supported systems.

Author Contributions: Conceptualization, R.R. and E.E.G.; methodology, E.E.G.; validation, E.E.G. and R.R.; formal analysis, R.R., E.E.G., J.L., P.B.-P., J.J.A.-G., D.H.G., and R.G.; investigation, R.R. and E.E.G.; resources, R.R., P.B.-P., J.J.A.-G., and R.G.; data curation, E.E.G.; writing—original draft preparation, R.R. and E.E.G.; writing—review and editing, R.R., E.E.G., J.L., P.B.-P., J.J.A.-G., and D.H.G.; funding acquisition, R.R.

Funding: This research received no external funding.

Acknowledgments: E. González acknowledges the scholarship provided by CONACyT. R. Rangel acknowledges the CIC-UMSNH project 2019. The authors thank W. Cauich for technical support in the XPS and SEM analyses, D. Aguilar for DRX analysis, and J. Bante for Raman spectroscopy analysis. The authors thank LANBIO-CINVESTAV and FOMIX-Yucatán 2008-108160 Conacyt LAB-2009-01-123913, 292692, 294643 projects.

Conflicts of Interest: The authors declare no conflict of interest.

References

1. Tit, N.; Said, K.; Mahmoud, N.M.; Kouser, S.; Yamani, Z.H. Ab-initio investigation of adsorption of CO and CO₂ molecules on graphene: Role of intrinsic defects on gas sensing. *Appl. Surf. Sci.* **2017**, *394*, 219–230. [[CrossRef](#)]
2. Zhao, Y.; Hu, J.; Tan, Z.; Liu, T.; Weilin, Z.; Li, X.; Huang, C.; Wang, S.; Huang, Z.; Ma, W. Ambient carbon monoxide and increased risk of daily hospital outpatient visits for respiratory diseases in Douguan, China. *Sci. Total Environ.* **2019**, *668*, 254–260. [[CrossRef](#)] [[PubMed](#)]
3. Ivanov, K.I.; Kolentsova, E.N.; Dimitrov, D.Y.; Avdeev, G.; Tabakova, T. Alumina supported copper-manganese catalysts for combustion of exhaust gases: Catalysts characterization. In Proceedings of the XIII International Conference on Chemical Engineering and Applications, Hong Kong, 27–28 August 2015.
4. Dey, S.; Dhal, G.C. Materials progress in the control of CO and CO₂ emission at ambient conditions: An overview. *Mater. Sci. Energy Technol.* **2019**, *2*, 607–623. [[CrossRef](#)]
5. Rangel, R.; Maya-Yescas, R.; García, R. Novel [Ce_{1-x}La_xO₂, La_{2-y}Ce_yO₃]/Bi₂Mo_{0.9}W_{0.1}O₆ catalysts for CO oxidation at low temperature. *Catal. Sci. Technol.* **2012**, *2*, 639–642. [[CrossRef](#)]
6. Keulks, G.W.; Hall, J.L.; Suzuki, C.D. The catalytic oxidation of propylene: IV. Preparation and characterization of a-bismuth molybdate. *J. Catal.* **1974**, *34*, 79–97. [[CrossRef](#)]
7. Trifiro, F.; Hoser, H.; Scarle, R.D. Relationship between structure and activity of mixed oxide as oxidation catalysts. I. Preparation and solid-state reactions of Bi-molybdates. *J. Catal.* **1972**, *25*, 12–24. [[CrossRef](#)]
8. Rastogi, R.P.; Singh, A.; Shukla, C.S. Kinetics and mechanism of solid-state reaction between bismuth(III) oxide and molybdenum(VI) oxide. *J. Solid State Chem.* **1982**, *42*, 136–148. [[CrossRef](#)]
9. Le, M.T.; Bac, L.H.; van Driessche, I.; Hoste, S.; van Well, W.J.M. The synergy effect between gamma and beta phase of bismuth molybdate catalysts: Is there any relation between conductivity and catalytic activity? *Catal. Today* **2008**, *131*, 566–571. [[CrossRef](#)]
10. Le, M.T.; van Craenenbroeck, J.; van Driessche, I.; Hoste, S. Bismuth molybdate catalysts synthesized using spray drying for the selective oxidation of propylene. *Appl. Catal. A Gen.* **2003**, *249*, 355–364. [[CrossRef](#)]
11. Carrazán, S.R.G.; Martín, C.; Mateos, R.; Rives, V. Influence of the active phase structure Bi-Mo-Ti-O in the selective oxidation of propene. *Catal. Today* **2006**, *112*, 121–125. [[CrossRef](#)]
12. Moro-oka, Y.; Ueda, W. Multicomponent bismuth molybdate catalyst: A highly functionalized catalyst system for the selective oxidation of olefin. *Adv. Catal.* **1994**, *40*, 233–273.
13. Schuh, K.; Kleist, W.; Høj, M.; Trouillet, V.; Beato, P.; Jensen, A.D.; Patzke, G.R.; Grunwaldt, J.D. Selective oxidation of propylene to acrolein by hydrothermally synthesized bismuth molybdates. *Appl. Catal. A Gen.* **2014**, *482*, 145–156. [[CrossRef](#)]
14. Brazdil, J.F.; Toft, M.A.; Lin, S.S.Y.; McKenna, S.T.; Zajac, G.; Kaduk, J.A.; Golab, J.T. Characterization of bismuth-cerium-molybdate selective propylene ammoxidation catalysts. *Appl. Catal. A Gen.* **2015**, *495*, 115–123. [[CrossRef](#)]
15. Rangel, R.; López, J.L.C.; Espino, J.; Núñez-González, R.; Bartolo-Pérez, P.; Gómez-Cortés, A.; Díaz, G. Estudio del efecto de diferentes soportes mixtos en la actividad catalítica y las características estructurales de catalizadores de Bi₂Mo_xW_{1-x}O₆. *Rev. Int. Contam. Ambient.* **2014**, *30*, 841–848.
16. Park, J.H.; Shin, C.H. Influence of the catalyst composition in the oxidative dehydrogenation of 1-butene over BiV_xMo_{1-x} oxide catalysts. *Appl. Catal. A Gen.* **2015**, *495*, 1–7. [[CrossRef](#)]
17. Joo, S.H.; Park, J.Y.; Renzas, J.R.; Butcher, D.R.; Huang, W.; Somorjai, G.A. Size effect of ruthenium nanoparticles in catalytic carbon monoxide oxidation. *Nano Lett.* **2010**, *10*, 2709–2713. [[CrossRef](#)] [[PubMed](#)]
18. Yamaguchi, K.; Mizuno, N. Supported ruthenium catalyst for the heterogeneous oxidation of alcohols with molecular oxygen. *Angew. Chem. Int. Ed.* **2002**, *114*, 4538–4542. [[CrossRef](#)]
19. Satsuma, A.; Yanagihara, M.; Ohyama, J.; Shimizu, K. Oxidation of CO over Ru/Ceria prepared by self-dispersion of Ru metal powder into nano-sized particle. *Catal. Today* **2013**, *201*, 62–67. [[CrossRef](#)]

20. Gaállová, J.; Barbier, J.; Rossignol, S. Ruthenium versus platinum on cerium materials in wet air oxidation of acetic acid. *J. Hazard. Mater.* **2010**, *181*, 633–639. [[CrossRef](#)] [[PubMed](#)]
21. Kim, H.Y.; Lee, H.M.; Henkelman, G. CO oxidation mechanism on CeO₂-supported Au nanoparticles. *J. Am. Chem. Soc.* **2011**, *134*, 1560–1570. [[CrossRef](#)] [[PubMed](#)]
22. Haruta, M.; Yamada, N.; Kobayashi, T.; Iijima, S. Gold catalysts prepared by coprecipitation for low-temperature oxidation of hydrogen and of carbon monoxide. *J. Catal.* **1989**, *115*, 301–309. [[CrossRef](#)]
23. Zhang, R.; Lu, K.; Zong, L.; Tong, S.; Wang, X.; Feng, G. Gold supported on ceria nanotubes for CO oxidation. *Appl. Surf. Sci.* **2017**, *416*, 183–190. [[CrossRef](#)]
24. Acosta, B.; Smolentseva, E.; Beloshapkin, S.; Rangel, R.; Estrada, M.; Fuentes, S.; Simakov, A. Gold supported on ceria nanoparticles and nanotubes. *Appl. Catal. A Gen.* **2012**, *449*, 96–104. [[CrossRef](#)]
25. Fonseca, J.; Royer, S.; Bion, N.; Pirault-Roy, L.; do Carmo Rangel, M.; Duprez, D.; Epron, F. Preferential CO oxidation over nanosized gold catalysts supported on ceria and amorphous ceria-alumina. *Appl. Catal. B Environ.* **2012**, *128*, 10–20. [[CrossRef](#)]
26. Aneghi, E.; Boaro, M.; Colussi, S.; de Leitenburg, C.; Trovarelli, A. Ceria-based materials in catalysis: Historical perspective and future trends. In *Handbook of the Physics and Chemistry of Rare Earths*; Bünzli, J.C., Pecharsky, V., Elsevier, B.V., Eds.; Elsevier: Amsterdam, The Netherlands, 2016; Volume 50, pp. 209–242. [[CrossRef](#)]
27. Ansari, S.A.; Khan, M.M.; Ansari, M.O.; Kalathil, S.; Lee, J.; Cho, M.H. Band-gap engineering of CeO₂ nanostructure using an electrochemically active biofilm for visible light applications. *RSC Adv.* **2014**, *4*, 16782–16791. [[CrossRef](#)]
28. Wu, T.S.; Chen, Y.W.; Weng, S.C.; Lin, C.N.; Lai, C.H.; Huang, Y.J.; Jeng, H.T.; Chang, S.L.; Soo, Y.L. Dramatic band gap reduction incurred by dopant coordination rearrangement in Co-doped nanocrystals of CeO₂. *Sci. Rep.* **2017**, *7*, 2–8. [[CrossRef](#)] [[PubMed](#)]
29. Spezzati, G.; Benavidez, A.D.; DeLaRiva, A.T.; Su, Y.; Hofmann, J.P.; Asahina, S.; Olivier, E.J.; Neethling, J.H.; Miller, J.T.; Datye, A.K.; et al. CO oxidation by Pd supported on CeO₂ (100) and CeO₂ (111) facets. *Appl. Catal. B Environ.* **2019**, *243*, 36–46. [[CrossRef](#)]
30. Li, J.; Liu, X.; Sun, Z.; Sun, Y.; Pan, L. Novel yolk-shell structure bismuth rich bismuth molybdate microsphere for enhanced visible-light photocatalysis. *J. Colloid Interface Sci.* **2015**, *452*, 109–115. [[CrossRef](#)] [[PubMed](#)]
31. Panagiotopoulou, P.; Verykios, X.E. Mechanistic aspects of the low temperature steam reforming of ethanol over supported Pt catalysts. *Int. J. Hydrogen Energy* **2012**, *37*, 16333–16345. [[CrossRef](#)]
32. Ferrer, V.; Finol, D.; Ramos, M. Caracterización química y actividad catalítica de óxidos mixtos soportados basados en cerio. *Ciencia* **2010**, *18*, 209–219.
33. Ratova, M.; Kelly, P.J.; West, G.T.; Xia, X.; Gao, Y. Deposition of visible light active photocatalytic bismuth molybdate thin films by reactive magnetron sputtering. *Materials* **2016**, *9*, 67–80. [[CrossRef](#)] [[PubMed](#)]
34. Ayame, A.; Uchida, K.; Iwataya, M.; Miyamoto, M. X-ray photoelectron spectroscopic study on α - and γ -bismuth molybdate surfaces exposed to hydrogen, propene, and oxygen. *Appl. Catal. A Gen.* **2002**, *227*, 7–17. [[CrossRef](#)]
35. Mun, C.; Ehrhardt, J.J.; Lambert, J.; Madic, C. XPS investigations of ruthenium deposited onto representative inner surfaces of nuclear reactor containment buildings. *Appl. Surf. Sci.* **2007**, *253*, 7613–7621. [[CrossRef](#)]
36. Yeung, H.; Chan, H.; Takoudis, C.G.; Weaver, M.J. High-pressure oxidation of ruthenium as probed by surface-enhanced raman and x-ray photoelectron spectroscopies. *J. Catal.* **1997**, *172*, 336–345. [[CrossRef](#)]
37. Prusty, D.; Pathak, A.; Mukherjee, M.; Mukherjee, B.; Chowdhury, A. TEM and XPS studies on the faceted nanocrystals of Ce_{0.8}Zr_{0.2}O₂. *Mater. Charact.* **2015**, *100*, 31–35. [[CrossRef](#)]
38. Aguilar-Guerrero, V.; Lobo-Lapidus, R.J.; Gates, B.C. Genesis of cerium oxide supported gold catalyst for CO oxidation: Transformation of mononuclear gold complexes into clusters as characterized by x-ray absorption spectroscopy. *J. Phys. Chem. C* **2009**, *113*, 3259–3269. [[CrossRef](#)]
39. Kosacki, I.; Petrovsky, V.; Anderson, H.U. Raman spectroscopy of nanocrystalline ceria and zirconia thin films. *J. Am. Ceram. Soc.* **2002**, *85*, 2646–2650. [[CrossRef](#)]
40. Bulushev, D.; Yuranov, I.; Suvorova, E.; Buffat, P.; Kiwi-Minsker, L. Highly dispersed gold on activated carbon fibers for low-temperature CO oxidation. *J. Catal.* **2004**, *224*, 8–17. [[CrossRef](#)]
41. Santos, V.P.; Carabineiro, S.A.C.; Bakker, J.J.W.; Soares, O.S.G.P.; Chen, X.; Pereira, M.F.R.; Órfão, J.J.M.; Figueiredo, J.L.; Gascon, J.; Kapteijn, F. Stabilized gold on cerium-modified cryptomelane: Highly active in low-temperature CO oxidation. *J. Catal.* **2014**, *309*, 58–65. [[CrossRef](#)]

42. Adhikari, R.; Joshie, B.; García, R.N.; de la Rosa, E.; Lee, W.S. Microwave hydrothermal synthesis and infrared to visible upconversion luminescence of Er³⁺/Yb³⁺ co-doped bismuth molybdate nanopowder. *J. Lumin.* **2016**, *145*, 866–871. [[CrossRef](#)]
43. Sleight, A.; Chen, H. Structure of Bi₂Mo₂O₉: A selective oxidation catalyst. *J. Solid State Chem.* **1986**, *63*, 70–75.
44. Casaletto, M.P.; Longo, A.; Martorana, A.; Prestianni, A.; Venezia, A.M. XPS study of supported gold catalysts: The role of Au⁰ and Au⁺⁸ species as active sites. *Surf. Interface Anal.* **2006**, *38*, 215–218. [[CrossRef](#)]
45. Piotrowski, T.; Accinno, D.J. Metallography of the precious metals. *Metallography* **1977**, *10*, 243–289. [[CrossRef](#)]
46. Carabineiro, S.A.C.; Silva, A.M.T.; Draić, G.; Tavares, P.B.; Figueiredo, J.L. Gold nanoparticles on ceria supports for the oxidation of carbon monoxide. *Catal. Today* **2010**, *154*, 21–30. [[CrossRef](#)]
47. Amano, F.; Nogami, K.; Abe, R.; Ohtani, B. Preparation and characterization of bismuth tungstate polycrystalline flake-ball particles for photocatalytic reactions. *J. Phys. Chem. C* **2008**, *112*, 9320–9326. [[CrossRef](#)]
48. Liao, P.C.; Mar, S.Y.; Ho, W.S.; Huang, Y.S.; Tiong, K.K. Characterization of RuO₂ thin films deposited on Si by metal-organic chemical vapor deposition. *Thin Solid Film.* **1996**, *287*, 74–79. [[CrossRef](#)]
49. Mukherjee, D.; Rao, B.G.; Reddy, B.M. CO and soot oxidation activity of doped ceria: Influence of dopants. *Appl. Catal. B Environ.* **2016**, *197*, 105–115. [[CrossRef](#)]
50. Qadir, K.; Joo, S.H.; Mun, B.S.; Butcher, D.R.; Renzas, J.R.; Aksoy, F.; Liu, Z.; Somorjai, G.A.; Park, J.Y. Intrinsic relation between catalytic activity of CO oxidation on Ru nanoparticles and Ru oxides uncovered with ambient pressure XPS. *Nano Lett.* **2012**, *12*, 5761–5768. [[CrossRef](#)] [[PubMed](#)]
51. Venkataswamy, P.; Jampaiah, D.; Mukherjee, D.; Aniz, C.U.; Reddy, B.M. Mn-doped ceria solid solutions for CO oxidation at lower temperatures. *Catal. Lett.* **2016**, *146*, 2105–2118. [[CrossRef](#)]
52. Mandapaka, R.; Madras, G. Zinc and platinum co-doped ceria for WGS and CO oxidation. *Appl. Catal. B Environ.* **2017**, *211*, 137–147. [[CrossRef](#)]
53. Zanella, R. Metodologías para la síntesis de nanopartículas: Controlando forma y tamaño, Mundo Nano. *Rev. Interdiscip. Nanocienc. Nanotecnol.* **2012**, *5*, 69–81.
54. Duan, Y.; Li, Z.; Li, Y.; Zhang, Y.; Li, L.; Li, J. New insight of the Mars-van Krevelen mechanism of the CO oxidation by gold catalyst on the ZnO (101) surface. *Comput. Theor. Chem.* **2017**, *1100*, 28–33. [[CrossRef](#)]
55. Zhang, S.; Li, X.; Chen, B.; Zhu, X.; Shi, C.; Zhu, A. CO oxidation activity at room temperature over Au/CeO₂ catalysts: Disclosure of induction period and humidity effect. *ACS Catal.* **2014**, *4*, 3481–3489. [[CrossRef](#)]
56. Kimling, J.; Maier, M.; Okenve, B.; Kotaidis, V.; Ballot, H.; Plech, A. Turkevich method for gold nanoparticle synthesis revisited. *J. Phys. Chem. B* **2006**, *110*, 15700–15707. [[CrossRef](#)] [[PubMed](#)]
57. Bueno-López, A.; Krishna, K.; Makkee, M.; Moulijn, J.A. Active oxygen from CeO₂ and its role in catalyzed soot oxidation. *Catal. Lett.* **2005**, *99*, 203–205. [[CrossRef](#)]

